energies

MDPI

Article

Numerical Simulation Analysis of the Temperature Field of Molten Salt Linear Fresnel Collector

Linggang Kong [1,2,*], Yuan Niu [2], Duojin Fan [1], Minsen Shi [2] and Ziyi Zheng [2]

[1] Engineering Research Center for Photothermal Energy Storage Integrated Energy System, Lanzhou Jiaotong University, Lanzhou 730070, China; 19829358894@163.com
[2] National Engineering Research Center for Technology and Equipment of Environmental Deposition, Lanzhou Jiaotong University, Lanzhou 730070, China; 12232065@stu.lzjtu.edu.cn (Y.N.); ddidg1@163.com (M.S.); 15865471238@163.com (Z.Z.)
* Correspondence: konglg@lzjtu.edu.cn

Abstract

A complex operating environment and high operating temperature lead to the uneven temperature field distribution of key components of the molten salt Linear Fresnel collector in a way that compromises the collector's safety and stability. To investigate the influence of different working conditions on the temperature field of the molten salt Linear Fresnel collector under multi-physical field conditions, this study develops a three-dimensional numerical model based on ANSYS that integrates the loading of solar radiation and thermal–fluid coupling, compares and verifies the accuracy of the model through the collector field data of the actual operation, and systematically analyzes the distribution characteristics of the receiver tube and outlet temperature field and its rule of change. The results show that temperatures of the receiver tube and exit during operation exhibit pronounced non-uniform distribution characteristics, in which the inlet flow rate of the molten salt and intensity of solar irradiation have the most critical influence on the temperature distribution throughout the receiver tube and its exit, and the heat transfer temperature difference between the molten salt and heat conduit wall is reduced as the inlet temperature raises, which makes the receiver tube and molten salt outlet temperature gradient slightly reduced. This study not only supplements and improves the numerical simulation study of the molten salt Linear Fresnel collector under complex working conditions but also reveals the distribution law of the temperature field between the receiver tube and the outlet, which provides adequate numerical support for the safe and stable operation of the collector.

Keywords: molten salt Linear Fresnel; numerical simulation; solar radiation load; heat flow coupling; temperature field

check for updates

Academic Editor: Tapas Mallick

Received: 25 September 2025
Revised: 22 October 2025
Accepted: 30 October 2025
Published: 4 November 2025

Citation: Kong, L.; Niu, Y.; Fan, D.; Shi, M.; Zheng, Z. Numerical Simulation Analysis of the Temperature Field of Molten Salt Linear Fresnel Collector. *Energies* **2025**, *18*, 5815. https://doi.org/10.3390/en18215815

Copyright: © 2025 by the authors. Licensee MDPI, Basel, Switzerland. This article is an open access article distributed under the terms and conditions of the Creative Commons Attribution (CC BY) license (https://creativecommons.org/licenses/by/4.0/).

1. Introduction

In light of the increasingly severe global energy crisis and climate change, developing green, clean, and efficient renewable energy technologies has become the core research direction in today's energy field [1]. Because it is a renewable energy source that does not harm the environment and has plenty of reserves, solar energy occupies a strategic position in the renewable energy system [2,3]. Concentrated Solar Power (CSP) [4,5] focuses solar radiation on the collector through a concentrator, generates high temperature thermal energy, and converts it to electricity through a thermal recycling system, which has attracted much attention because of its clean and pollution-free power generation process, stable power generation capacity, high energy conversion efficiency, and good energy storage

characteristics. As a core heat collection method in solar power generation technology [6], the Linear Fresnel concentrator, with its significant advantages such as simple structure, low cost, and easy modular arrangement, has shown a broad application prospect in medium and high temperature thermal energy applications and solar thermal power generation systems [7,8]. As a heat transfer medium, molten salt has obvious advantages over other materials, such as a higher operating temperature, simple system operation and maintenance, and no need for a salt/oil heat exchanger [9]. However, the complex operating conditions and high operating temperatures lead to a high degree of randomness in the outlet temperature. It has a significant impact on the steady operation of the system as well as its overall effectiveness [10,11].

The complex environmental factors during the operation of the collector have always been of interest to researchers. Baba et al. [12] intended to provide an innovative, streamlined temporary model for evaluating the changing performance of a non-vacuum single-pipe receiver tube integrated with a composite parabola collector. An examination was conducted into the receiver's behavior in both steady-state and transient scenarios, with a focus on the effect of critical factors such as the mass flow rate and type of heating liquid, receiver length, and absorber pipe thickness. In identical operational circumstances, higher efficiencies can be achieved with synthetic oil fluids, and higher outlet temperatures can be achieved with molten salts. To study how construction and operational variables influence receiver efficiency, Karim et al. [13] created a 2-D hydrodynamic simulation of a solar energy receiver that concentrates light by direct absorption in a molten salt nanofluid at high temperatures. The results demonstrate that the Carnot efficiency improves when the receiver length, sunlight concentrator power, and intake speed decrease. Yu et al. [14] built a heat transmission simulation of a novel solar collector arrangement utilizing a trough-type V-cavity absorber, analyzed the impact of diverse environmental variables on collector efficiency and outlet temperature, and used the comparison results to adjust the model for various meteorological ambient conditions. The effect of thermal flux and the temperature distribution of trough collectors on system performance was numerically investigated based on Fluent software by Halimi [15]. Lu [16] constructed a 3-D numerical model containing multi-physics field coupling, such as fluid flow and thermal transfer, and systematically analyzed the influence laws of essential operational factors, including the inlet temperature and reactant feed rate. By comparing the performance of the two, it is found that the circumferential distribution characteristics of solar flux have a decisive influence on the uniformity of temperature and reaction fields. Wang and Qiu [17] used the finite volume method to numerically calculate the property of a finned molten salt heat absorber. And the validity of the proposed model was verified by checking the outcomes against the experimental results of the power station. Then, the model was utilized to gain the optimum structure of the finned heat absorber through parameter optimization.

As for the study and numerical validation of heat transfer performance for various collectors, the establishment of three-dimensional numerical models and the combination of the finite element method and computational fluid dynamics are widely used. Asayesh et al. [18] used the receiver geometrical parameters as the optimization object, and the combination of the COMSOLMultiphysics simulation and analysis and prototype experiments significantly improved the system's optical and thermal efficiency. The optimized receiver achieved a heat flux absorption of more than 10,000 W/m^2 under peak solar radiation conditions, with a working fluid temperature increase of about 22 °C and a maximum outlet temperature of more than 47 °C. Alcalde-Morales [19] developed a cavity heat absorber for a Fresnel linear concentrator based on a two-dimensional hydrodynamic solution performed by Fluent software. This study presents a detailed analysis of the thermodynamic properties of the air within the Fresnel concentrator cavity. It models the

performance of the Linear Fresnel concentrator using a robust Monte Carlo ray tracing (MCRT) method, achieving a prediction accuracy of over 97%. Qiu and He [20] developed and investigated the new Linear Fresnel collector using a vacuum pipe, with sun salt as the thermal transfer fluid. To estimate the system's radiative transmittance, a 3-D optical model was created using the Monte Carlo ray tracing approach. Combining MCRT and the finite volume approach allowed the authors to examine its thermal performance. Yang [21] and Rungasamy [22] also used the same modeling approach to simulate the collector performance with more than 97% accuracy. Hong et al. [23] numerically studied a trough-type solar collector's thermal and flow characteristics. A non-uniform focused thermal flux was applied to the absorber pipe, and the finite volume approach was used to model turbulence in the receiver pipe. Rimar [24] design experiment depends on the variables of the collector structure's material, the absorption characteristics of the device, the associated materials and structures, the features of the thermal transfer fluid, and the configuration of the volumetric flow rate. The fluctuation of the incident radiant energy flux can also be delineated. Nokhosteen [25] proposed a novel hybrid computational method for simulating the thermal behavior of a collector during diurnal operation. The method is based on a previously developed intrinsic orthogonal decomposition method based on a resistive network for simulating the operating hours when the solar radiation value is greater than zero. Tengah et al. [26] based their study on the ANSYS platform to construct a refined computational fluid dynamics model and thoroughly investigate the enhancement mechanism of hollow twisted strip inserts on the energy transfer efficiency of absorber tubes. Qusay et al. [27] systematically carried out an experimental study on the thermal performance of a Linear Fresnel solar concentrator based on the meteorological conditions of different seasons in the Baghdad area and numerically verified the experimental results generated from computational fluid dynamics that validate the accuracy of the CFD approach to the concentrator's performance evaluation.

In summary, the multiple coupling of environmental conditions and operating parameters significantly impacts the thermal transfer performance and temperature field distribution of Linear Fresnel collectors, and molten salt, as a high-temperature heat transfer medium, shows a unique advantage in system efficiency and heat storage performance. Still, its sensitivity to fluctuations in the operating conditions makes the outlet temperature show strong instability, which poses a challenge for the reliability of the collector operation. Although the existing studies have made significant progress in revealing the heat transfer mechanism, numerical modeling, and experimental validation, a systematic and in-depth investigation into the distribution law of the receiver tube and outlet temperature field of the Linear Fresnel collector utilizing molten salt as a working medium under complex operational conditions remains insufficient. This study constructed a three-dimensional numerical simulation based on ANSYS with integrated solar radiation and thermal–fluid coupling. This study systematically examines the influence of critical operating parameters, including solar irradiation intensity, molten salt inlet flow rate, and inlet temperature, on the temperature distribution within the suction tube and the characteristics of the outlet temperature, providing theoretical understanding and practical recommendations for improving the stability and performance of the Linear Fresnel collector.

2. Model Description

2.1. Physical Model

The molten salt Linear Fresnel collector is mainly constructed of three parts: the main reflector column, the vacuum collector tube, and the Compound Parabolic Concentrator (CPC). The principle is mainly that the sun's light is gathered by the main reflector to the receiver, where part of the reflected light is directly focused on the collector tube, and

the remaining part of the CPC reflector is reflected through the second reflection after projection to the collector tube. The collector tube absorbs the solar radiation and then heats the molten salt in the receiver tube to transform the solar power into heat energy.

The CPC is shown in Figure 1, assuming that the inside diameter of a receiver tube of the vacuum collector is r_1, the sum of the outer diameter of the glass outer pipe and the gap is r_2. The receiving half-angle is θ_A, then the CPC cross-section curve in the plane right-angled coordinate system is expressed as [28]

$$\begin{cases} x = r_1 sin\theta - \rho cos\theta \\ y = -r_1 cos\theta - psin\theta \end{cases} \quad (1)$$

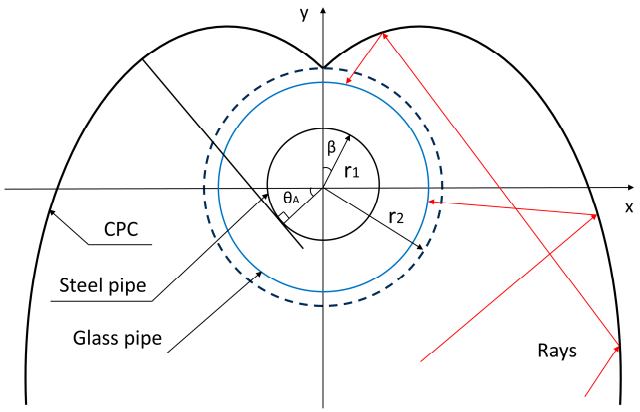


Figure 1. Schematic representation of CPC ray tracing.

θ is the angle variable parameter.

$$\rho = r_1(\theta + \beta),\ arccos\left(\frac{r_1}{r_2}\right) \le \theta \le \frac{\pi}{2} + \theta_A \quad (2)$$

$$\rho = \frac{r_1\left[\frac{\pi}{2} + \theta + \theta_A + 2\beta - cos(\theta - \theta_A)\right]}{1 + sin(\theta - \theta_A)} \quad (3)$$

$$\frac{\pi}{2} + \theta_A \le \theta \le \frac{3\pi}{2} - \theta_A \quad (4)$$

$$\beta = \sqrt{\left(\frac{r_2}{r_1}\right)^2 - 1} - \arccos\left(\frac{r_1}{r_2}\right) \quad (5)$$

As shown in Figure 2, assuming that the maximum acceptance half-angle of the CPC in the mirror field is θ_{max}, the receiver is placed at the height H from the plane where the mirrors are located; the width of the mirrors is D; the distance between the center of the nth reflector and the center of the mirror field is Q_n, and the angle between Q_n and the horizontal plane is βn (the angle of inclination); the spacing of the adjacent mirrors is S_n; the incidence of sunlight is α; and where θ_n is the angle at which the reflected light is the incident. The axes of rotation of all the mirrors occupy the identical plane horizontally. The angle of incidence of sunlight α changes with time and causes the angle of inclination of the mirrors in the mirror field β_n to change continuously. Given the sunlight incidence angle α and the receiver height H, the relationship between the parameters of the unshaded mirror field arrangement is [29]

$$\tan(\pi - \alpha - 2\beta_n) = \frac{H}{Q_n} \quad (6)$$

$$S_n = \frac{D}{2}\left[\frac{\sin\beta_n + \sin\beta_{n-1}}{\tan\alpha} + \cos\beta_n + \cos\beta_{n-1}\right] \quad (7)$$

$$Q_n = Q_{n-1} + S_n, n \geq 1 \tag{8}$$

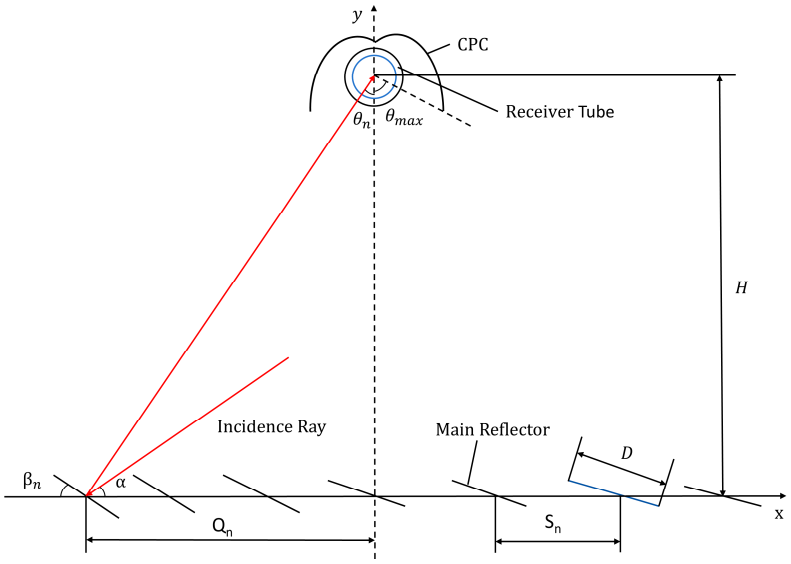


Figure 2. Schematic representation of molten salt Linear Fresnel collector concentrating light.

The angle of incidence α of sunlight at any given moment could be determined using this formula:

$$\alpha = \frac{\pi}{2} + \omega. \tag{9}$$

where ω is the solar time angle, which is specified as noon $\omega = 0$, morning $\omega < 0$, and afternoon $\omega > 0$, and the value is equal to the time (hours) from noon multiplied by 15°.

Based on the above geometric and model parameters of the components in the collector system, the physical model is constructed using the Space Claim modeling tool in ANSYS, as illustrated by Figure 3.

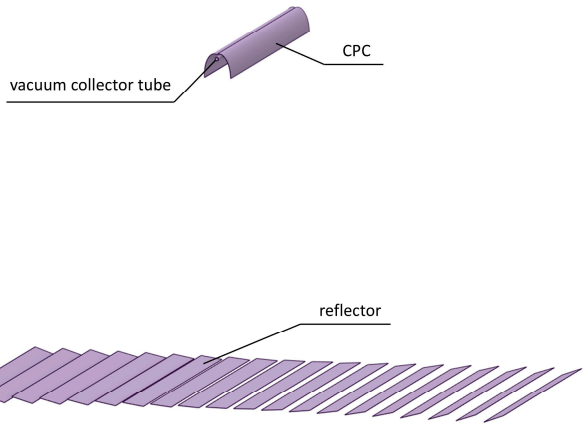


Figure 3. Structural model of molten salt Linear Fresnel collector.

2.2. Calculation Model

The Reynolds number range of (4497, 17,978) is calculated from the molten salt's average flow rate, and the receiver tube's inner diameter indicates that the flow is fully turbulent [30]. Therefore, the RNG k-ε turbulence model was used to characterize the flow. This model is more accurate in dealing with the vortex flow and strong shear regions than the standard k-ε model and works well with the intricate flow field under investigation here; the physical model is numerically simulated using Fluent software in ANSYS 2023R1 to solve the governing equations based on the conservation of mass, momentum, and energy

to obtain the molten salt's temperature and velocity field distributions in the receiver tube. The basic governing equations solved include the continuity equation, momentum equation, and energy equation [31], which are mathematically expressed as follows:

Continuity equation:

$$\frac{\partial}{\partial x_i}(\rho u_i) = 0 \tag{10}$$

Momentum equation:

$$\frac{\partial}{\partial x_i}(\rho u_i u_j) = -\frac{\partial P}{\partial x_j} + \frac{\partial}{\partial x_j}\left[(\mu_t + \mu)\left(\frac{\partial u_i}{\partial x_j} + \frac{\partial u_j}{\partial x_i}\right) - \frac{2}{3}(\mu_t + \mu)\left(\frac{\partial u_k}{\partial x_k}\delta_{ij}\right)\right] \tag{11}$$

Energy equation:

$$\frac{\partial}{\partial x_i}(\rho u_i T) = \frac{\partial}{\partial x_i}\left[\left(\frac{\mu}{Pr} + \frac{\mu_t}{\sigma_T}\right)\frac{\partial T}{\partial x_i}\right] + S_R \tag{12}$$

K equations:

$$\frac{\partial}{\partial x_i}(\rho u_i k) = \frac{\partial}{\partial x_i}\left[\left(\mu + \frac{\mu_t}{\sigma_k}\right)\frac{\partial k}{\partial x_i}\right] + G_k - \rho\varepsilon \tag{13}$$

The ε-equation:

$$\frac{\partial}{\partial x_i}(\rho u_i \varepsilon) = \frac{\partial}{\partial x_i}\left[\left(\mu + \frac{\mu_t}{\sigma_\varepsilon}\right)\frac{\partial \varepsilon}{\partial x_i}\right] + \frac{\varepsilon}{k}(c_1 G_k - c_2 \rho\varepsilon) \tag{14}$$

Eddy viscosity:

$$\mu_t = C_\mu \rho \frac{k^2}{\varepsilon} \tag{15}$$

In the above equation, ρ is the density; u_i is the velocity component; C_μ is used to calculate the turbulent viscosity, the empirical coefficient, which is often taken to be 0.09 in the calculation; δ_{ij} is the Kronecker operator; Pr is the molecular Prandtl number; ε is the dissipation rate; and σ_T is the turbulence temperature Prandtl number, which is usually taken to be 0.9.

$$G_k = \mu_t \sum_i \sum_j \left(\frac{\partial u_i}{\partial x_j}\right)\left(\frac{\partial u_i}{\partial x_j} + \frac{\partial u_j}{\partial x_i}\right) \tag{16}$$

Where G_k is the term for turbulent kinetic energy produced by mean shear.

$$S_R = \kappa\left(4\sigma T^4 - \sum_{m=1}^{N_\Omega} w_m I_m\right) + S_b \tag{17}$$

Where S_R is the radiation source term per unit volume and represents the net energy exchange between the participating medium and the radiation field. In the discrete coordinate (DO) model, the calculation is carried out by solving the radiative transfer equation along the direction of the discrete angle to obtain the radiant intensity I_m in each direction, and then summing up the incident radiation according to the directional weights.

Since the boundary conditions in the simulation model of this paper are also different, the setting of boundary conditions must also be analyzed specifically. Among them, the outer glass tube surface boundary is a mixed boundary condition, the glass tube is a semi-transparent medium with a thickness of 2 mm, the emissivity of the outer boundary of the glass pipe is 0.86, and the emissivity of the surface coating of the metal pipe is 0.08. A heat-flow boundary is established by exchanging the fluid within the pipe with the receiver tube. The remaining borders are designated as insulating boundaries.

Incident solar intensity:

$$I\left(\vec{r_0}, \vec{s_\odot}\right) = \frac{DNI}{\pi} \tag{18}$$

Direct Normal Irradiance (DNI) is normal direct irradiance, a custom parameter; π indicates the average distribution of solar radiation within the hemispherical steradian angle.

Solar source term:

$$S_b\left(\vec{r}, \vec{s}\right) = I_b\, \delta\left(\vec{s} - \vec{s_\odot}\right) \tag{19}$$

where S_b is an external solar light source that serves as an input term to the DO equation; I_b *is* determined by Direct Normal Irradiance (DNI). After solving the DO equation to obtain the intensity of radiation in each direction, the radiant energy source term S_R is calculated by integration.

For the selection of the radiation model, considering the radiation of the semi-transparent medium in the model, as well as the diffuse reflection, specular reflection, and other physical properties, only the DO model [32] meets the requirements of the simulation calculation. Moreover, the model can deal with the system's radiative heat transfer process and wall radiation. Meanwhile, the Solar Load Model is introduced to simulate the heating effect of solar radiation on the receiver tube. Based on the set geographic location, date, time, and solar irradiance parameters, the intensity and direction of solar radiation are calculated and introduced as a source term in the energy equation. The integrated approach can simulate the heat transfer mechanism of the collector under actual solar irradiation conditions, which is suitable for the analysis of the light–heat coupling process of the multi-reflector and collector tube multilayer structure in the molten salt Linear Fresnel concentrator collector. The simulation and simulation process involve heat exchange and energy transfer, so it is necessary to introduce the energy equation.

2.3. Grid Generation

To guarantee the precision and numerical convergence of the simulation outcomes, it is essential to develop a rational and high-quality grid layout. In this paper, the Fluent Meshing tool in ANSYS is used to mesh the 3-D physical model of the molten salt Linear Fresnel collector. Taking into account the substantial size disparities across the system's constituent sections and sensitivity of distinct regions to the mesh accuracy, a partitioned encryption strategy [33] is adopted to set differentiated mesh size parameters for the critical components.

The collector area, as the primary heat transfer component of the system, comprises the fluid zone, vacuum insulation layer, metallic receiver tube, and glass outer tube, among others, in which heat–flow coupling characteristics of the fluid–solid interface have high requirements for the mesh accuracy. To verify the precision of the heat transfer and fluid flow simulation, the minimum size of the surface mesh in this area is 4 mm, the maximum size is 10 mm, and the mesh growth rate is 1.2. Based on this, the body mesh is generated, and the structured hexahedral cells are preferentially used to take into account both the mesh quality and computational efficiency. In contrast, the CPC and reflector regions mainly assume the function of reflecting and guiding solar radiation, and the thermal coupling is weak, so their surfaces are moderately encrypted to meet the accuracy of the radiation model. The surface mesh size of this area is set from 4 mm to 50 mm, and the growth rate is also 1.2, with the goal of achieving a balance between the calculation of ray tracing and the efficiency of the mesh. The overall meshing details are seen in Figure 4.

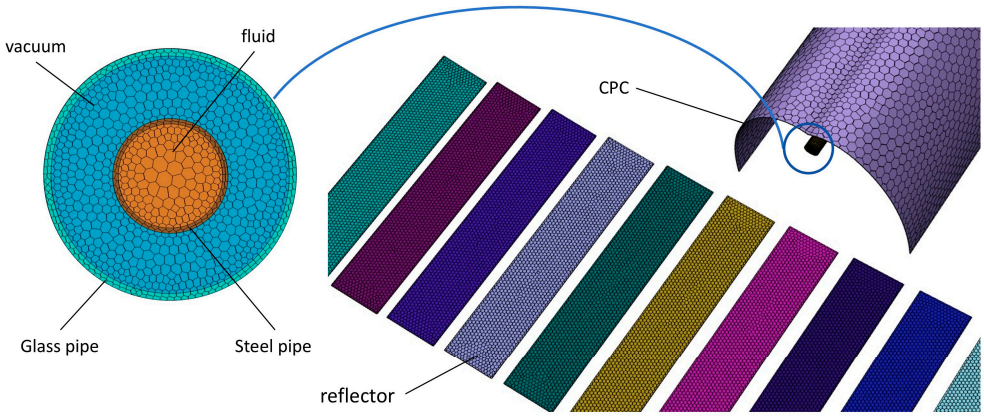


Figure 4. Schematic diagram of model meshing.

After the overall meshing process, the total number of generated body grid cells is 4,145,397, and the mesh quality is evaluated using skewness and orthogonal quality metrics. The results show that the maximum skewness is 0.73, and the minimum orthogonal quality is 0.83. This indicates that the generated grid met high-quality standards and could satisfy the numerical stability and accuracy requirements for subsequent heat-flow coupling calculations.

2.4. Grid Independence Test

To ensure the accuracy and stability of the numerical calculations, the grid independence of the Linear Fresnel collector model is verified. Based on the same physical model and boundary conditions, three magnitude grid types are generated, as shown in Table 1. The computational results show that when the number of grids exceeds 400,000 cells, the temperature change at the outlet of the heat-absorbing pipe is less than 0.5%, and the difference in the wall temperature distribution is negligible, indicating that the numerical solution has reached grid independence. The Test I density grid is finally selected for subsequent simulation and analysis to ensure the accuracy and efficiency of the calculation.

Table 1. Grid independence test.

Test	Number of Elements	T_{out} (°C)	Deviation
Test I	4,145,397	325.491	_
Test II	8,619,532	325.504	0.034%
Test III	12,872,517	325.502	0.016%

3. Simulation

3.1. Simulation Analysis

The numerical model is set up in a basic manner, and computations are performed using a pressure-based steady-state solver. The pressure-velocity coupling is handled using the Coupled algorithm, and the equations of momentum, energy, and turbulence are discretized in the second-order upwind format. The turbulence is modeled using the k-ω SST model to account for wall resolution and separated flow cases. The radiative heat transfer is modeled using the DO model to calculate the heat exchange between direct solar radiation and the surface.

The Discrete Ordinates (DO) model is a general and highly accurate method for solving the radiation problem. The model obtains the radiation intensity distribution at any point in space by discretizing the angular domain into a number of fixed directions (ordinates) and solving the Radiation Transport Equation (RTE) in each direction, which is not only able to

deal with the coupled effects of absorption, scattering and emission in the participating media, but also applicable to high temperature flow, complex geometry and multiple reflection boundary conditions. The DO model can not only deal with the coupled effects of absorption, scattering, and emission in the participating medium but can also be applied to high-temperature flows, complex geometries, and multiple reflection boundary conditions. Moreover, it can directly introduce the Solar Load Model and accurately model the collector system with the actual solar incidence angle, azimuth angle and surface optical properties. Most importantly, it can take into account both specular and diffuse reflections, thus more realistically describing the radiative coupling between mirrors and the receiver tube.

The irradiation intensity, location latitude and longitude, time zone, and simulation time are set. Secondly, the boundary is established with a constant inlet mass flow rate in the heat absorber tube and a static pressure outlet. The primary reflector is set as an optical mirror with a reflectivity of 0.95. The outer surface of the receiver tube is set as an optical absorption–emission boundary with a surface absorptivity of 0.9 and an emissivity of 0.85. The convection heat exchange boundary is used between the exposed wall and the environment.

With a group of receiver tube units (length 8 m) as the simulation object, the boundary conditions are set to direct a radiation intensity of 1000 W/m^2, heat transfer fluid entrance flow rate of 0.15 m/s, entrance temperature of 290 °C, and ambient temperature of 28 °C. The energy flow density distribution of the receiver tube, the temperature profile of the receiver tube, and the temperature and velocity fields of the molten salt outlet cross-section are obtained, as shown in Figures 5–8.

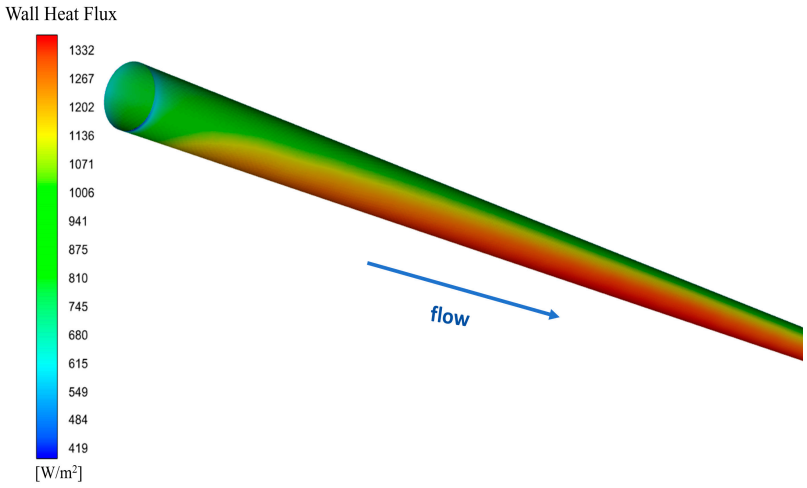


Figure 5. Heat flux distribution of receiver tube.

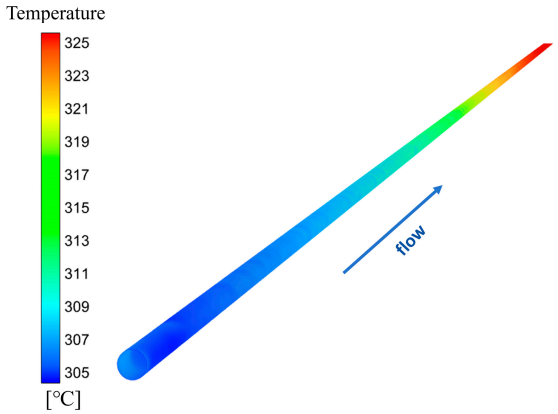


Figure 6. Temperature distribution of receiver tube.

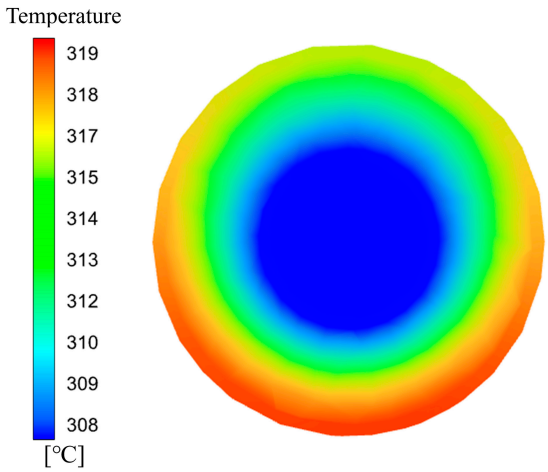


Figure 7. Temperature distribution of molten salt outlet.

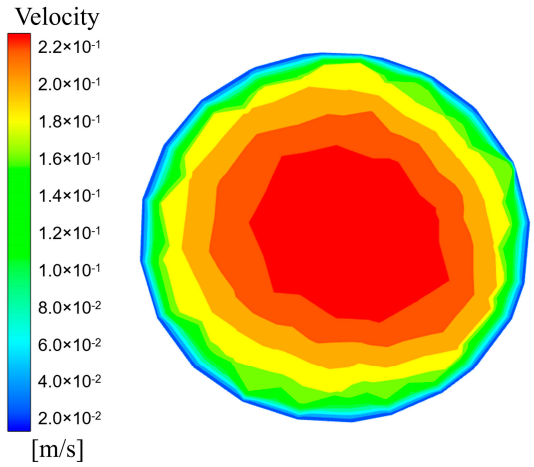


Figure 8. Velocity distribution of molten salt outlet.

From Figure 5, it can be seen that the heat flux distribution on the surface of the metal receiver tube is not uniform; the largest heat flux region reaches 1332 W/m^2, the smallest region is only 480 W/m^2, and the inhomogeneity of the thermal flux on the surface of the receiver tube is substantial. The surface temperature distribution on the receiver tube is seen in Figure 6. Receiver tube surfaces do not have a uniform distribution of temperature in both the axial and radial directions due to the fact that they absorb various amounts of solar light. Along the direction of the molten salt flow, the temperature difference on the surface of the receiver tube gradually rises, mainly because of the low temperature of molten salt at the entrance of the thermal pipe, the heat absorption capacity, and the temperature gradient of the wall at the entrance of the thermal tube is less. With the warming of molten salt, the thermal absorption capacity decreases at the exit of the receiver tube, so the temperature gradient of the wall at the exit of the receiver tube is larger. The temperature gradient of the receiver tube has a large impact on the life of the collector, so it is extremely important to simulate the temperature field on the surface of the thermal tube under varying circumstances. Figure 7 displays the temperature distribution of the molten salt outlet cross-section. The temperature of the mass is higher near the circumference of the cross-section, i.e., near the wall of the receiver tube, and lower in the center of the cross-section, i.e., in the center of the receiver tube. Figure 8 illustrates that the velocity distribution at the outlet of the molten salt shows a roughly symmetrical distribution but is not perfectly symmetrical due to the presence of buoyancy effects. It is maximal at its center of the axis and diminishes toward the suction pipe wall due to wall resistance. Due

to the fluctuations in the temperature and flow speed sectors throughout the collector's operation, which significantly influence its thermal efficiency and stability, it is essential to examine the variables impacting the collector's flow field.

3.2. Simulation Model Verification

The Lanzhou Dacheng Dunhuang Molten Salt Linear Fresnel 50 MW Solar Power Generation Demonstration Project is the inaugural commercial molten salt Linear Fresnel solar power plant to commence formal operations globally (located in Dunhuang, longitude 94.1° E, latitude 40.08° N), and the panoramic view of the solar power plant's concentrating light and heat collection system is shown in Figure 9. The physical model parameters of the project are displayed in Table 2, and the material thermophysical parameters are displayed in Table 3. By comparing and analyzing field data from the related operating circumstances and setting the model according to the real variables in the project's collection site, we can validate the veracity of the simulation findings. As shown in Table 4, simulation data and actual field data for six cases were selected for comparison, and the relative deviation in temperature rise was calculated. The results show that the relative deviation of temperature rise is within 7% under various working conditions, from the low-temperature stage to the high-temperature stage, which demonstrates the overall reliability of the model and meets the requirement for exploring the effects of various working conditions on the receiver tube and outlet temperature field.



Figure 9. Panoramic view of concentrator and collector system of Solar Power Generation Demonstration Project.

Table 2. Molten salt Linear Fresnel collector model parameters.

Structural Parameters	Unit	Numerical Value
Mirror width of the main reflector D	mm	780
Number of columns of the main reflector	Columns	20
Distance between columns of the main reflector S_n	mm	250
Collector center height H	m	12.5
Outer radius of the metal receiver inner tube of the collector r_1	mm	90
Outer radius of the glass outer tube of collector r_2	mm	145
Distance from the center of the collector to the CPC tip r_3	mm	160
Maximum receiving half-angle of CPC θ_{max}	°	42

Table 3. Physical parameters of the materials.

	Solar Salt (300 °C)	Glass Outer Tube (High Transmittance, Low-Iron Glass)	Metal Inner Tube (Stainless Steel)
Density (kg/m^3)	1863	2220	8030
Specific heat capacity (KJ/(kg·K))	1.504	830	502.48
Thermal conductivity (W/m·K)	0.501	1.15	16.27

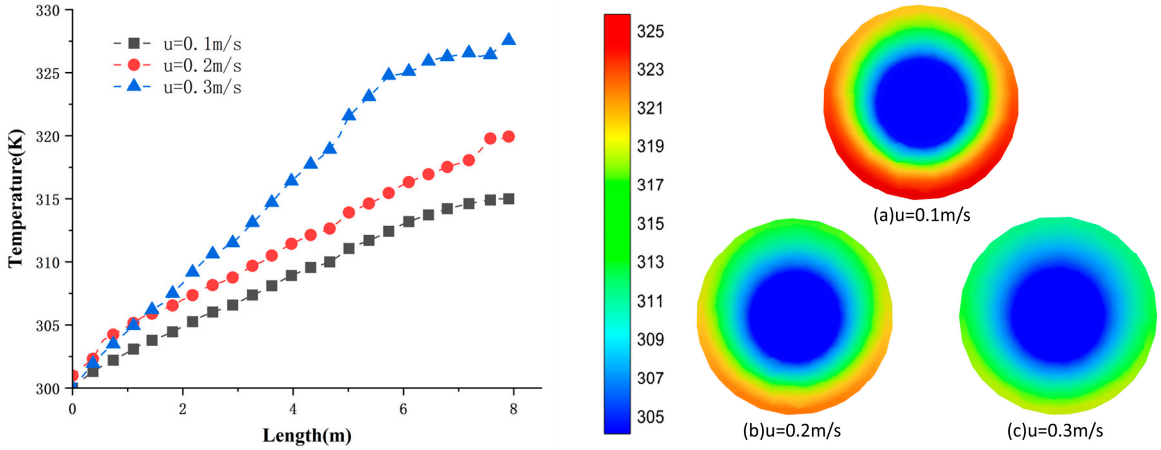
Table 4. Comparison of simulation data with actual field data.

CASE	DNI (W/m^2)	T_e (°C)	Flow Rate (m/s)	T_{in} (°C)	$T_{f,out}$ (°C)	$T_{s,out}$ (°C)	Relative Deviation (%)
Case1	435.34	16.85	0.94	307.56	323.18	322.43	4.92
Case1	551.26	18.34	1.49	293.81	312.92	311.94	5.26
Case1	612.84	23.92	1.82	398.92	423.11	424.54	5.74
Case1	762.99	26.18	2.18	377.14	399.34	456.92	6.93
Case1	880.48	30.63	2.35	512.73	535.71	534.94	3.41
Case1	922.51	32.17	2.27	498.73	526.44	528.02	5.88

4. Influence of Operating Conditions on the Thermal Performance of the Collector

4.1. Inlet Flow Rate

Modify the intake velocity of the heat transfer medium in the heat absorption tube while maintaining the direct irradiation intensity of 1000 W/m^2 and the initial temperature of the fluid at 300 °C so as to guarantee that the heat transfer medium within the heat absorption tube is in a fully turbulent state during flow, the inlet velocity of the medium is 0.1 m/s~0.3 m/s, and the pipe of the wall temperature is obtained, along with the distribution of the length of the pipe, as seen in Figure 10A. The temperature field of the molten salt outlet section is shown in Figure 10B.



(**A**) (**B**)

Figure 10. Temperature variations along the length of the receiver tube wall at different inlet flow rates (**A**); temperature field at different inlet flow rates of molten salt outlet (**B**).

Figure 10A demonstrates the outcome of varying incoming flow rates on the temperature distribution of the absorber tube wall, with a single collector unit as the object of study; when the molten salt inlet flow rate raised from 0.1 m/s to 0.3 m/s, the change in temperature of the absorber tube wall is very obvious, the absorption tube wall maximum temperature decreased from 328 °C to 317 °C, and the temperature gradient across the pipe wall decreased from 25 °C to 17 °C, which shows that, with the increase in the flow rate, the temperature of the wall and the temperature gradient decreased more obviously. With the increase in velocity, the wall temperature and temperature gradient exhibited a more pronounced reduction.

Figure 10B illustrates the outcome of varying inlet flow rates on the temperature distribution of the molten salt outlet cross-section. At flow velocities of 0.1 m/s, 0.2 m/s, and 0.3 m/s, the temperatures that vary among the entrance and exit of molten salt are 25 °C, 20 °C, and 16 °C, respectively. Correspondingly, the temperature variation at the molten salt outlet cross-section is 19 °C, 15 °C, and 9 °C. This indicates that a rise in velocity diminishes both the temperature difference between the inlet and outlet of the molten salt and the temperature gradient across the cross-section, resulting in a more uniform outlet temperature.

Although the outlet temperature exhibits a slight decrease, the increased mass flow rate enables a larger amount of absorbed solar energy to be transported away within the molten salt per unit time. This process effectively mitigates the thermal load on the absorber wall and reduces the local temperature gradients within the solid domain. Moreover, the intensified internal flow motion of the molten salt enhances convective mixing. It promotes a more uniform temperature distribution along the flow direction, thereby facilitating more efficient overall heat removal from the receiver tube.

4.2. Inlet Temperature

The direct irradiation intensity was kept at 1000 W/m^2 and the molten salt inlet velocity at 0.15 m/s, while all other conditions remained unchanged. Only the inlet temperature of the medium in the receiver tube was varied. Specifically, simulations were conducted with inlet temperatures of 300 °C, 320 °C, and 340 °C. The wall temperature distribution along the length of the receiver tube is shown in Figure 11A, while the temperature field at the molten salt outlet section is presented in Figure 11B.

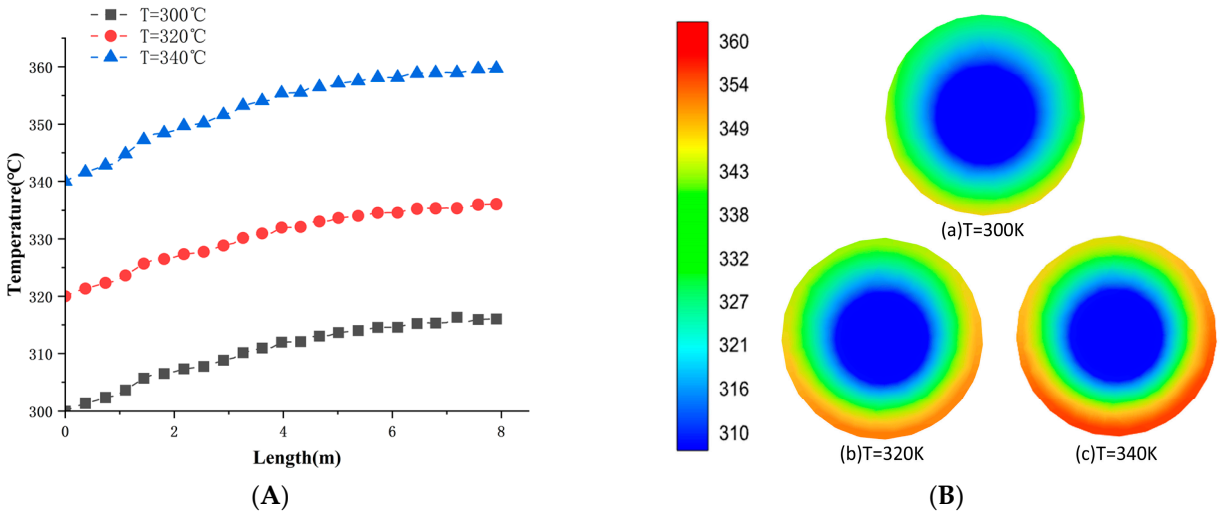


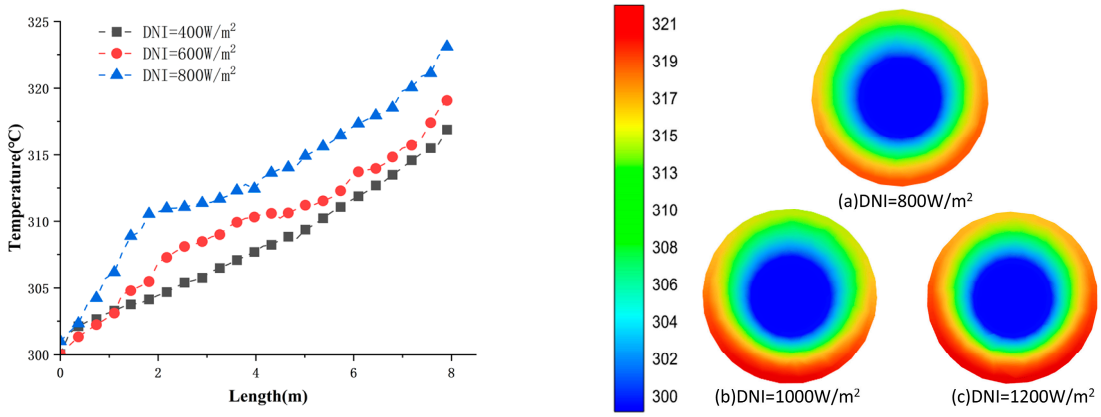
Figure 11. Temperature variations along the length of the receiver tube wall at different inlet temperatures (**A**); temperature field at different inlet temperatures of molten salt outlet (**B**).

From Figure 11A, when the inlet temperatures are 300 °C, 320 °C, and 340 °C, respectively, the maximum temperature difference in the absorber tube wall is 14 °C, 16 °C, and 21 °C, respectively. As the temperature rises, the temperature differential of the absorber pipe wall is somewhat elevated, mainly because of the high inlet temperature; the temperature difference between the bulk flow and the absorber tube wall is small, and the convective heat exchange coefficient will be reduced.

Figure 11B shows the effect of inlet temperature on the temperature field of the molten salt outlet section; when the inlet temperature is 300 °C, 320 °C, 340 °C, respectively, the disparity in temperature between the inlet and outlet is 20 °C, 18 °C, 16 °C, respectively, and the maximum temperature difference between the molten salt outlet section is 9 °C, 15 °C, and 19 °C; and with a rise in the molten salt entrance temperature, the temperature difference between the import and export of molten salt reduces slightly, and temperature inhomogeneity of the outlet section of molten salt enhances, mainly due to the decrease in the heat exchange and its effect on the molten salt and the wall surface with the high temperature as a result of the reduced thermal transfer action between the wall and molten salt. Reduced energy transfer between the wall's surface and the high-temperature molten salt is the main reason, here.

4.3. Irradiation Intensity

Under constant conditions of a heat transfer medium import velocity of 0.15 m/s and import temperature of 300 °C, only the intensity of direct solar radiation is varied. The direct solar radiation intensities range from 400 W/m^2 to 800 W/m^2. In light of these details, the distribution of the receiver tube wall temperature along the perimeter of the receiver tube is obtained, as seen in Figure 12A. The temperature field at molten salt exit cross-section is shown in Figure 12B.



(**A**) (**B**)

Figure 12. Temperature variations along the length of the receiver tube wall at different irradiation intensities (**A**); temperature field at different irradiation intensities of molten salt outlet (**B**).

Figure 12A shows the effect of Direct Normal Irradiance (DNI) on the temperature distribution of the absorber tube wall. Direct Normal Irradiance significantly impacts changes in the tube wall temperature. For the absorber pipe, the outside heat flux and wall temperature are both affected by the intensity of Direct Normal Irradiance. In the range of 400 W/m^2 to 800 W/m^2, which is the amount of direct solar radiation, the absorber tube's temperature anomaly rises from 15 °C to 25 °C.

Figure 12B shows the effect of solar direct radiation intensity on the temperature of the molten salt outlet cross-section. When the direct radiation intensity is 400 W/m^2,

600 W/m^2, and 800 W/m^2, the temperature difference between the entrance and exit of the receiver tube is 13 °C, 15 °C, and 19 °C, respectively, and the temperature difference at the outlet cross-section is 9 °C, 10 °C, and 12 °C, respectively. As the solar direct irradiance intensity increases, the disparity temperature between the entry and exit points of the molten salt in the collector significantly increases, while the temperature difference at the exit cross-section slightly increases.

5. Conclusions

This paper establishes a three-dimensional heat transfer model for a molten salt Linear Fresnel collector by integrating the solar radiation load with ANSYS software. The impact of essential working situation variables like the molten salt inlet flow rate, inlet temperature, and direct solar irradiation intensity on the distribution of the temperature field of the receiver tube and outlet are analyzed. The results show that the surface temperature of the metal receiver tube is unevenly distributed along the axial direction, and the temperature of the tube wall gradually increases along the molten salt flow direction. Simultaneously, the temperature distribution of the molten salt outlet cross-section has radial inhomogeneity, i.e., as compared to the location in the middle of the circle, the temperature outside the circle is much greater, forming a decreasing temperature gradient from the outside to the inside, and the homogeneity is significantly affected by the operating conditions. Among them, the inlet flow rate possesses the most critical influence on the temperature field of the receiver tube and the molten salt outlet. As the inlet flow rate rises from 0.1 m/s to 0.3 m/s, the temperature difference between the wall of the receiver tube decreases by 11 °C; the temperature difference between the entrance and exit of the molten salt reduces by 8 °C; and although there is a temperature disparity between the outlet sections, it decreases by 52%. The elevated flow velocity amplifies the turbulent heat transfer and flow perturbation and significantly improves the uniformity of the temperature field between the tube wall and the outlet. The increase in molten salt's inlet temperature resulted in an upward shift in the temperature of the receiver tube wall. Still, the temperature difference between the wall and the bulk flow decreased, leading to a decrease in the local thermal transfer capacity and raises in the temperature difference in the outlet cross-section by 10 °C, which indicated that higher inlet temperatures weakened the homogeneity of the temperature field at the outlet of the molten salt. The increase in direct solar irradiation intensity significantly increased the overall temperature rise in the molten salt, reflecting the key role of irradiation intensity in determining the heat load level of the system; however, this process also exacerbated the inhomogeneity of the temperature field at the tube wall and the outlet cross-section, which demonstrated the paradoxical relationship between the heat load level and the temperature homogeneity.

Author Contributions: Conceptualization, L.K.; methodology, L.K. and Y.N.; software, Y.N.; validation, Y.N.; formal analysis, L.K. and Y.N.; investigation, M.S.; resources, D.F.; data curation, D.F.; writing—original draft preparation, Y.N.; writing—review and editing, Z.Z.; visualization, M.S.; project administration, L.K.; funding acquisition, L.K. All authors have read and agreed to the published version of the manuscript.

Funding: This research was in part funded by the National Natural Science Foundation of China, No. 52266012 and the Science and Technology Planning Project of Gansu Province, 24CXGF006 and the Science and Technology Planning Project of Lanzhou City, 20240324.

Data Availability Statement: The original contributions presented in this study are included in the article. Further inquiries can be directed to the corresponding author.

Acknowledgments: All the authors thank Lanzhou Dacheng Science and Technology Co., Ltd. for their experimental platform, and the National Energy Administration of China and Gansu Provincial Development and Reform Commission for their strong support.

Conflicts of Interest: The authors declare no conflicts of interest.

Abbreviations

The following abbreviations are used in this manuscript:

CSP	Concentrated Solar Power
MCRT	Monte Carlo Ray Tracing
CFD	Computational Fluid Dynamics
CPC	Compound Parabolic Concentrator
RNG	Renormalization Group
3D	Three Dimensions
DO	Discrete Ordinates
DNI	Direct Normal Irradiance
Re	Reynolds Number

References

1. Maka, A.O.; Ghalut, T.; Elsaye, E. The pathway towards decarbonisation and net-zero emissions by 2050: The role of solar energy technology. *Green Technol. Sustain.* **2024**, *2*, 100107. [CrossRef]
2. Rashid, F.L.; Aljibori, H.S.; Mohammed, H.I.; Ameen, A.; Ahmad, S.; Hamida, M.B.B.; Al-Rubaye, A.H. Recent advances and developments of the application of hybrid nanofluids in parabolic solar collector energy systems and guidelines for future prospects. *J. Eng. Res.* **2024**, *in press*. [CrossRef]
3. Hussain, B.; Naqvi, S.A.A.; Anwar, S.; Usman, M. Effect of wind and solar energy production, and economic development on the environmental quality: Is this the solution to climate change? *Gondwana Res.* **2023**, *119*, 27–44. [CrossRef]
4. Damarseckin, S.; Atiz, A.; Karakilcik, M. Solar pond integrated with parabolic trough solar collector for producing electricity and hydrogen. *Int. J. Hydrogen Energy* **2024**, *52*, 115–126. [CrossRef]
5. Awan, A.B.; Khan, M.; Zubair, M.; Bellos, E. Commercial parabolic trough CSP plants: Research trends and technological advancements. *Sol. Energy* **2020**, *211*, 1422–1458. [CrossRef]
6. Montanet, E.; Rodat, S.; Falcoz, Q.; Roget, F. Influence of topography on the optical performances of a Fresnel linear asymmetrical concentrator array: The case of the eLLO solar power plant. *Energy* **2023**, *274*, 127310. [CrossRef]
7. Su, X.; Luo, C.; Ji, J.; Xi, X.; Chen, X.; Yu, Y.; Wen, J.; Zou, W. Assessment of photovoltaic performance and carbon emission reduction potential of bifacial PV systems for regional grids in China. *Sol. Energy* **2024**, *269*, 112367. [CrossRef]
8. Zhang, X.; Li, J.; Chen, J.; Chen, F. Preliminary investigation on optical performance of linear fresnel lens coupled compound parabolic concentrator. *Energy* **2023**, *278*, 127910. [CrossRef]
9. Bonini, V.R.; Starke, A.R.; da Silva, A.K. A technical-economic analysis and optimization of a direct molten salts linear Fresnel plant. *J. Braz. Soc. Mech. Sci. Eng.* **2024**, *46*, 510. [CrossRef]
10. Nualsing, D.; Pannucharoenwong, N.; Echaroj, S.; Rattanadecho, P. Investigation of molten salts incorporated with anodic aluminum oxide as thermal energy storage fluid on heat transfer efficiency. *Case Stud. Therm. Eng.* **2023**, *49*, 103258. [CrossRef]
11. Podila, K.; Li, C.; Azih, C.; Chen, Q. Modelling of heat transfer in a molten salt loop using computational fluid dynamics. *Prog. Nucl. Energy* **2023**, *164*, 104880. [CrossRef]
12. Baba, Y.F.; Al Mers, A.; Ajdad, H.; Bouatem, A.; Faik, A.; Idrissi, B.B. No-vacuum mono-tube compound parabolic collector receiver for linear Fresnel concentrator: Numerical and experimental approach for dynamic behavior assessment. *Energy Convers. Manag.* **2022**, *268*, 115986. [CrossRef]
13. Karim, M.; Arthur, O.; Yarlagadda, P.K.; Islam, M.; Mahiuddin, M. Performance investigation of high temperature application of molten solar salt nanofluid in a direct absorption solar collector. *Molecules* **2019**, *24*, 285. [CrossRef]
14. Bie, Y.; Li, M.; Chen, F.; Królczyk, G.; Li, Z. Heat transfer mathematical model for a novel parabolic trough solar collecting system with V-shaped cavity absorber. *Sustain. Cities Soc.* **2020**, *52*, 101837. [CrossRef]
15. Halimi, M.; El Amrani, A.; Chaanaoui, M.; Amrani, A.-i.; Oumachtaq, A.; Messaoudi, C. Investigation of parabolic trough collector receiver with U-pipe exchanger using a numerical approach: Towards temperature non-uniformity optimization. *Appl. Therm. Eng.* **2023**, *234*, 121335. [CrossRef]
16. Lu, B.; Liu, T.; Yan, X.; Zheng, Z.; Liu, Q. A new solar mid-and-low temperature receiver/reactor with linear Fresnel reflector. *Appl. Therm. Eng.* **2023**, *226*, 120216. [CrossRef]

17. Wang, W.-Q.; Qiu, Y.; Li, M.-J.; He, Y.-L.; Cheng, Z.-D. Coupled optical and thermal performance of a fin-like molten salt receiver for the next-generation solar power tower. *Appl. Energy* **2020**, *272*, 115079. [CrossRef]
18. Asayesh, M.; Kasaeian, A.; Mirzahosseini, S.A.H.; Saraei, A. A semi-enclosed cavity receiver for linear fresnel reflectors: Parametric analysis, CFD simulation and experimental study. *Appl. Therm. Eng.* **2025**, *278*, 127422. [CrossRef]
19. Alcalde-Morales, S.; Valenzuela, L.; Serrano-Aguilera, J.J. Heat losses in a trapezoidal cavity receiver of a linear Fresnel collector: A CFD approach. *Heliyon* **2023**, *9*, e18692. [CrossRef] [PubMed]
20. Qiu, Y.; He, Y.-L.; Cheng, Z.-D.; Wang, K. Study on optical and thermal performance of a linear Fresnel solar reflector using molten salt as HTF with MCRT and FVM methods. *Appl. Energy* **2015**, *146*, 162–173. [CrossRef]
21. Yang, N.; Liu, Q.; Xuan, J.; Wang, B.; Xing, L. Enhancing optical and thermohydraulic performance of linear Fresnel collectors with receiver tube enhancers: A numerical study. *Int. J. Heat Mass Transf.* **2024**, *231*, 125850. [CrossRef]
22. Rungasamy, A.; Craig, K.; Meyer, J.P. Comparative performance evaluation of candidate receivers for an etendue-conserving compact linear Fresnel mirror field. *Sol. Energy* **2022**, *231*, 646–663. [CrossRef]
23. Hong, K.; Yang, Y.; Rashidi, S.; Guan, Y.; Xiong, Q. Numerical simulations of a Cu–water nanofluid-based parabolic-trough solar collector. *J. Therm. Anal. Calorim.* **2021**, *143*, 4183–4195. [CrossRef]
24. Rimar, M.; Fedak, M.; Kulikov, A.; Kulikova, O.; Lopusniak, M. Analysis and CFD modeling of thermal collectors with a tracker system. *Energies* **2022**, *15*, 6586. [CrossRef]
25. Nokhosteen, A.; Sobhansarbandi, S. Numerical modeling and experimental cross-validation of a solar thermal collector through an innovative hybrid CFD model. *Renew. Energy* **2021**, *172*, 918–928. [CrossRef]
26. Tengah, N.N.A.B.; Sopian, K.; Kazem, H.A.; Chaichan, M.T.; Al-Waeli, A.H. Performance of a photovoltaic-thermal solar collector with hollow twisted ribbon inserted in absorber tubes: A theoretical and experimental study. *Sol. Energy* **2025**, *295*, 113541. [CrossRef]
27. Abdul-Ghafoor, Q.J.; Abed, S.H.; Kadhim, S.A.; Al-Maliki, M.A. Experimental and numerical study of a linear Fresnel solar collector attached with dual axis tracking system. *Results Eng.* **2024**, *23*, 102543. [CrossRef]
28. Oommen, R.; Jayaraman, S. Development and performance analysis of compound parabolic solar concentrators with reduced gap losses–oversized reflector. *Energy Convers. Manag.* **2001**, *42*, 1379–1399. [CrossRef]
29. Ma, J.; Wang, C.-L.; Zhou, Y.; Wang, R.-D. Optimized design of a linear Fresnel collector with a compound parabolic secondary reflector. *Renew. Energy* **2021**, *171*, 141–148. [CrossRef]
30. Rehman, S.; Zayed, M.E.; Irshad, K.; Menesy, A.S.; Kotb, K.M.; Alzahrani, A.S.; Alhems, L.M. Design, commissioning and operation of a large-scale solar linear Fresnel system integrated with evacuated compound receiver: Field testing, thermodynamic analysis, and enhanced machine learning-based optimization. *Sol. Energy* **2024**, *278*, 112785. [CrossRef]
31. Ahmadpour, A.; Dejamkhooy, A.; Shayeghi, H. Optimization and modelling of linear Fresnel reflector solar concentrator using various methods based on Monte Carlo Ray–Trace. *Sol. Energy* **2022**, *245*, 67–79. [CrossRef]
32. Lei, W.; Liu, J.; Zhao, J.; Qi, X.; Tai, C.; Zhang, L.; Li, A. Study of the application of solar chimneys combined with earth-air heat exchangers ventilation system (SEVS) in a solar greenhouse. *Energy* **2025**, *334*, 137537. [CrossRef]
33. Alsalame, H.A.M.; Sik, K.K.; Lee, G.H. Comparative Numerical and Experimental Analyses of Conical Solar Collector and Spot Fresnel Concentrator. *Energies* **2024**, *17*, 5437. [CrossRef]

Disclaimer/Publisher's Note: The statements, opinions and data contained in all publications are solely those of the individual author(s) and contributor(s) and not of MDPI and/or the editor(s). MDPI and/or the editor(s) disclaim responsibility for any injury to people or property resulting from any ideas, methods, instructions or products referred to in the content.